

Photoinduced Floquet higher-order Weyl semimetal in C_6 symmetric Dirac semimetals

Xin-Xin Xu(许欣欣), Zi-Ming Wang(王梓名), Dong-Hui Xu(许东辉), Chui-Zhen Chen(陈垂针)

Citation: Chin. Phys. B, 2024, 33 (**6**): 067801. DOI: 10.1088/1674-1056/ad4634
Journal homepage: http://cpb.iphy.ac.cn; http://iopscience.iop.org/cpb

What follows is a list of articles you may be interested in

Optical study of magnetic topological insulator $MnBi_4Te_7$

Zhi-Yu Liao(廖知裕), Bing Shen(沈冰), Xiang-Gang Qiu(邱祥冈), and Bing Xu(许兵)
Chin. Phys. B, 2024, 33 (**1**): 017802. DOI: 10.1088/1674-1056/ad08aa

Dynamically controlled asymmetric transmission of linearly polarized waves in VO_2-integrated Dirac semimetal metamaterials

Man Xu(许曼), Xiaona Yin(殷晓娜), Jingjing Huang(黄晶晶), Meng Liu(刘蒙), Huiyun Zhang(张会云), and Yuping Zhang(张玉萍)
Chin. Phys. B, 2022, 31 (**6**): 067802. DOI: 10.1088/1674-1056/ac4bd3

Broadband strong optical dichroism in topological Dirac semimetals with Fermi velocity anisotropy

J Lim(林镇杰), K J A Ooi(黄健安), C Zhang(涨潮), L K Ang(洪礼祺), Yee Sin Ang(洪逸欣)
Chin. Phys. B, 2020, 29 (**7**): 077802. DOI: 10.1088/1674-1056/ab928e

Gradient refractive structured NiCr thin film absorber for pyroelectric infrared detectors

Yunlu Lian(练芸路), He Yu(于贺), Zhiqing Liang(梁志清), Xiang Dong(董翔)
Chin. Phys. B, 2019, 28 (**6**): 067801. DOI: 10.1088/1674-1056/28/6/067801

Optical investigation of topological semimetal $SrMnSb_2$

Zi-Yang Qiu(邱子阳), Zhi-Yu Liao(廖知裕), Xiang-Gang Qiu(邱祥冈)
Chin. Phys. B, 2019, 28 (**4**): 047801. DOI: 10.1088/1674-1056/28/4/047801

RAPID COMMUNICATION

Photoinduced Floquet higher-order Weyl semimetal in C_6 symmetric Dirac semimetals

Xin-Xin Xu(许欣欣)[1], Zi-Ming Wang(王梓名)[2], Dong-Hui Xu(许东辉)[2,3,†], and Chui-Zhen Chen(陈垂针)[1,‡]

[1] *Institute for Advanced Study and School of Physical Science and Technology, Soochow University, Suzhou* 215006, *China*
[2] *Department of Physics and Chongqing Key Laboratory for Strongly Coupled Physics, Chongqing University, Chongqing* 400044, *China*
[3] *Center of Quantum Materials and Devices, Chongqing University, Chongqing* 400044, *China*

(Received 3 April 2024; revised manuscript received 29 April 2024; accepted manuscript online 2 May 2024)

Topological Dirac semimetals are a parent state from which other exotic topological phases of matter, such as Weyl semimetals and topological insulators, can emerge. In this study, we investigate a Dirac semimetal possessing sixfold rotational symmetry and hosting higher-order topological hinge Fermi arc states, which is irradiated by circularly polarized light. Our findings reveal that circularly polarized light splits each Dirac node into a pair of Weyl nodes due to the breaking of time-reversal symmetry, resulting in the realization of the Weyl semimetal phase. This Weyl semimetal phase exhibits rich boundary states, including two-dimensional surface Fermi arc states and hinge Fermi arc states confined to six hinges. Furthermore, by adjusting the incident direction of the circularly polarized light, we can control the degree of tilt of the resulting Weyl cones, enabling the realization of different types of Weyl semimetals.

Keywords: Dirac semimetals, Weyl semimetals, periodic driving, higher-order topology

PACS: 78.40.Kc, 03.65.Vf **DOI:** 10.1088/1674-1056/ad4634

1. Introduction

The study of topological semimetals[1,2] is a crucial area of modern condensed matter physics, primarily driven by the possibility of observing phenomena akin to those from the realm of relativistic physics within these materials. The novel macroscopic quantum phenomena they exhibit are not only of fundamental interest, but may hold potential for technological applications. Among diverse topological semimetals, three-dimensional (3D) topological Dirac semimetals (DSMs),[3,4] the 3D analogy of graphene, hold particular significance due to their distinctive feature of exhibiting linear dispersion around band crossing points. This characteristic, reminiscent of 3D massless Dirac fermions, arises from the presence of doubly degenerate bands that touch at specific points in momentum space. Besides time-reversal symmetry (TRS) and inversion symmetries, the stability of Dirac nodes in topological DSMs also requires additional crystalline symmetries, like rotational symmetries.[5,6]

Despite possessing topological invariants, the lack of a conventional bulk–boundary correspondence in topological DSMs sparked debate over their classification as a genuine topological phase of matter.[7–9] However, topological DSMs do serve as a parent phase for engineering other intriguing topological phases of matter, such as Weyl semimetal (WSM) or topological insulators. Recently, certain topological DSMs have been found to exhibit higher-order topological bulk-hinge correspondence. These topological DSMs demonstrate 1D hinge Fermi arc states that terminate on the projection of Dirac nodes, which are dubbed higher-order DSMs.[10–15]

Floquet engineering[16–18] has emerged as a powerful tool for realizing novel topological phases in quantum materials. It involves using time-periodic perturbations, such as light, to tailor band structures and topology of the quantum materials.[19–81] The periodic driving enables accessing non-equilibrium states that are difficult to obtain in static systems. A seminal example is illuminating graphene with circularly polarized light (CPL) to induce quantum Hall states.[24] The light effectively produces complex next-nearest neighbor hopping amplitudes, leading to the Haldane model of quantum anomalous Hall effect.[28] A recent experiment reported the evidence of nearly quantized Hall conductance associated with the photoinduced Floquet quantum anomalous Hall state in graphene.[82]

As the 3D analogy of graphene, CPL has been shown to create the Floquet WSM in topological DSMs by breaking TRS.[44,47,50,59] Moreover, a Floquet WSM state accommodating both surface Fermi arcs and higher-order hinge Fermi arcs can emerge in a fourfold rotational (C_4) symmetric topological DSM, related to the experimentally confirmed DSM material Cd_3As_2, under the irradiation of CPL.[78] Sixfold rotational (C_6) symmetric DSMs are another prototypical topological DSM. The first experimental verified topological DSM Na_3Bi[83] belongs to C_6 symmetric topological DSM. Recently, Na_3Bi is also predicted to host higher-order

†Corresponding author. E-mail: donghuixu@cqu.edu.cn
‡Corresponding author. E-mail: czchen@suda.edu.cn

© 2024 Chinese Physical Society and IOP Publishing Ltd

hinge Fermi arc states,[12,13,15] thus serving as a C_6 symmetric higher-order DSM candidate. The study of the Floquet topological phases in C_6 symmetric higher-order DSMs is desirable as it will provide an opportunity for the realization of controllable higher-order WSM[84–86] in solid materials.

In this work, we study the Floquet physics in C_6 symmetric higher-order DSM illuminated by off-resonant CPL. Within the framework of the Floquet theory, we derive an effective static Hamiltonian for the periodically driven DSM. Based on the effective Hamiltonian, we demonstrate that each of the pair of Dirac nodes evolves into a pair of Weyl nodes due to the breaking of time-reversal symmetry, giving rise to a Floquet WSM. The projections of each pair of Weyl nodes in the surface Brillouin zone are connected by a surface Fermi arc. Meanwhile, six hinge Fermi arcs reside on the hinges of a C_6 symmetric rod, connecting the projections of two adjacent Weyl nodes from different pairs. Moreover, for the CPL along the x and y directions, the tilting of the resulting Weyl cones can be controlled by adjusting the amplitude of light, which can give rise to a Floquet type-II WSM in a parent type-I DSM.

2. Undriven DSM model and Floquet theory

In this section, we introduce a four-band tight-binding model on a hexagonal lattice to describe the C_6 symmetric DSMs and provide a brief review of the Floquet theory. The basis vectors of the hexagonal lattice can be written as $\boldsymbol{a}_1 = (1,0,0)$, $\boldsymbol{a}_2 = (-\frac{1}{2}, \frac{\sqrt{3}}{2}, 0)$, $\boldsymbol{a}_3 = (0,0,1)$. Consequently, the momentum space is parameterized by $k_1 = k_x$, $k_2 = -\frac{1}{2}k_x + \frac{\sqrt{3}}{2}k_y$. The Hamiltonian in momentum space is given by[7,12]

$$H = \varepsilon_0(\boldsymbol{k})\Gamma_0 + \sum_{i=1}^{5} \varepsilon_i(\boldsymbol{k})\Gamma_i, \tag{1}$$

with

$$\begin{aligned}
\varepsilon_0(\boldsymbol{k}) &= m_0 + 2m_2\left[\cos k_1 + \cos k_2 + \cos(k_1+k_2)\right] \\
&\quad + 2m_1 \cos k_z, \\
\varepsilon_1(\boldsymbol{k}) &= \lambda\left[-2\sin k_1 + \sin k_2 - \sin(k_1+k_2)\right], \\
\varepsilon_2(\boldsymbol{k}) &= \sqrt{3}\lambda\left[\sin k_2 + \sin(k_1+k_2)\right], \\
\varepsilon_3(\boldsymbol{k}) &= M_0 + 2M_2\left[\cos k_1 + \cos k_2 + \cos(k_1+k_2)\right] \\
&\quad + 2M_1 \cos k_z, \\
\varepsilon_4(\boldsymbol{k}) &= \gamma \sin k_z\left[2\cos k_1 - \cos k_2 - \cos(k_1+k_2)\right], \\
\varepsilon_5(\boldsymbol{k}) &= \sqrt{3}\gamma \sin k_z\left[\cos k_2 - \cos(k_1+k_2)\right],
\end{aligned} \tag{2}$$

where the Γ matrices are defined as $\Gamma_0 = \tau_0 \otimes \sigma_0$, $\Gamma_i = \tau_3 \otimes \sigma_i$, with $i = 1,2,3$, $\Gamma_4 = \tau_1 \otimes \sigma_0$, $\Gamma_5 = \tau_2 \otimes \sigma_0$. Here τ_i and σ_j, with $i,j = 1,2$ and 3, are the Pauli matrices representing the spin and orbital degrees of freedom, respectively, while σ_0 and τ_0 are 2×2 identity matrices. The parameters m_0, M_0, m_1, m_2, M_1, M_2, λ, γ represent the onsite potential, mass term, and amplitudes of various hopping processes, respectively. The γ terms are responsible for producing the higher-order topology of DSMs. This four-band tight-binding model preserves inversion symmetry $\mathcal{I} = \tau_z\sigma_z$, TRS $\mathcal{T} = \mathrm{i}\tau_0\sigma_y\mathcal{K}$ ($\mathcal{K}$ is the complex conjugate operator), and crystalline symmetries such as $C_{2x} = \mathrm{i}\tau_y\sigma_y$ and $C_{6z} = \mathrm{i}\,\mathrm{e}^{\mathrm{i}\tau_z\pi/6} \otimes \mathrm{e}^{-\mathrm{i}\sigma_z\pi/6}$.

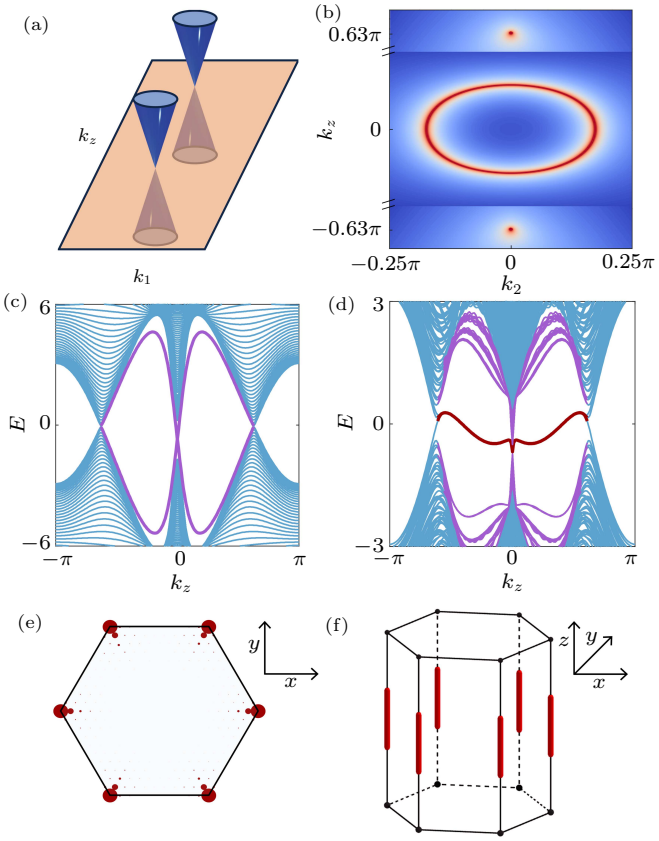


Fig. 1. Electronic structures and topological boundary states of the undriven DSM. (a) The schematic illustration of two bulk Dirac cones on the k_1–k_z plane of the DSM. (b) The surface local density of states (LDOS) with the semi-infinite boundary along the x direction when $E = 0$. The two red dots are the projections of the two bulk Dirac points. The red ring is the surface Fermi ring. (c) The surface band structure versus k_z for $k_x = 0$. The purple solid lines show the gapless surface state between two Dirac points. (d) The energy spectrum with open boundary conditions (OBCs) along the x and y directions. The solid purple lines show gapless surface states. The HOFA is marked by the solid red line between the projections of the bulk Dirac points. (e) The distribution of LDOS of HOFA of $k_z = 0.02\pi$ on the x–y plane. (f) The schematic illustration of distribution of HOFA in the real space. The model parameters are chosen as $M_0 = 4$, $M_1 = -2.5$, $M_2 = -1$, $\lambda = 1$, $\gamma = 5$, $m_0 = -0.4$, $m_1 = -0.1$, $m_2 = 0.05$.

The bulk energy spectrum of the model is given by $E = \varepsilon_0(\boldsymbol{k}) \pm \sqrt{\sum_i \varepsilon_i^2}$. The DSM model exhibits two Dirac points along the k_z axis, as illustrated in Fig 1(a), located at $\boldsymbol{K}_0 = (0,0,k_{z\pm}^0)$ with $k_{z\pm}^0 = \frac{\pm M_0 - m_0 \pm 6M_2 - 6m_2}{2(m_1 \mp M_1)}$. As shown in Fig. 1(b), this DSM features a closed Fermi ring, formed by a Dirac cone, in the surface Brillouin region due to its bulk topology characterized by a 2D Z_2 invariant. The spectrum of the Dirac cone is plotted in Fig. 1(c), revealing that the surface Dirac cone is located at $k_z = 0$. To unveil the higher-order topology of the DSM, Fig. 1(d) plots the spectrum of this model in a hexagonal rod geometry, showing the exis-

tence of higher-order Fermi arc (HOFA) states terminating on the Dirac point. Figure 1(e) depicts the density distribution of these HOFA states for a given k_z, where corner states exist on the hexagonal disk in the x–y plane. As k_z varies, the corner states extend to form HOFA states running along the hinge between two adjacent side planes, as illustrated in Fig. 1(f).

We apply a monochromatic CPL field with periodic time dependence and homogeneous spatial dependence to drive the DSM. The CPL can be described by a time-dependent vector potential $\boldsymbol{A}(\tau)=\boldsymbol{A}(\tau+T)$ with a time period $T=2\pi/\omega$, where ω is the frequency of light. The vector potential $\boldsymbol{A}(\tau)$ usually takes the form $[A_x\sin(\omega\tau+\varphi_1),A_y\sin(\omega\tau+\varphi_2),A_z\sin(\omega\tau+\varphi_3)]$, where A_x, A_y, and A_z represent the amplitudes of the potential vector along the x, y, and z directions, respectively, and φ_1, φ_2, and φ_3 are the initial phases. Alternatively, the vector potential can be expressed as $\boldsymbol{A}(\tau)=A(0,\eta\sin\omega\tau,\cos\omega\tau),A(\eta\sin\omega\tau,0,\cos\omega\tau)$ or $A(\eta\sin\omega\tau,\cos\omega\tau,0)$ with $\eta=\pm1$ labeling the handedness, representing CPL propagating along the x, y, and z directions, respectively. In this paper, we mainly introduce the case of CPL propagating along the z, x and y directions. In the presence of CPL, the hopping integrals of electrons between lattice sites $\boldsymbol{r}_j$ and $\boldsymbol{r}_k$ gain a phase factor, which can be characterized by the Peierls substitution

$$\tilde{t}_{jk}\to\tilde{t}_{jk}\,\mathrm{e}^{\mathrm{i}\frac{\hbar}{e}\boldsymbol{A}(\tau)\cdot(\boldsymbol{r}_k-\boldsymbol{r}_j)}. \tag{3}$$

As a result, the Hamiltonian becomes time-periodic, $H(\tau)=H(\tau+T)$. The Floquet theorem allows us to map the time-dependent Schrodinger equation $\mathrm{i}\partial_\tau|\Psi(\tau)\rangle=H(\tau)|\Psi(\tau)\rangle$ to a static one. The solutions to the Schrodinger equation take the form $|\Psi(\tau)\rangle=\mathrm{e}^{-\mathrm{i}\varepsilon\tau}|\Phi(\tau)\rangle$, where ε is the Floquet quasienergy and $|\Phi(\tau)\rangle=|\Phi(\tau+T)\rangle$ is the Floquet eigenvector. By performing a Fourier expansion $H(\tau)=\sum_m\mathrm{e}^{-\mathrm{i}m\omega\tau}H_m$ and $|\Phi(\tau)\rangle=\sum_m\mathrm{e}^{-\mathrm{i}m\omega\tau}|\Phi^m\rangle$ for the Hamiltonian and the Floquet eigenvector, the time-dependent Schrodinger equation is mapped to an infinite-dimensional eigenvalue equation in the extended Hilbert space[20]

$$\sum_m(H_{n-m}-m\omega\delta_{mn})|\Phi_\alpha^m\rangle=\varepsilon_\alpha|\Phi_\alpha^m\rangle, \tag{4}$$

where $H_{n-m}=\frac{1}{T}\int_0^T\mathrm{d}\tau\,\mathrm{e}^{\mathrm{i}(n-m)\omega\tau}H(\tau)$. Throughout, we concentrate on situations where electron transitions facilitated by photon absorption or emission are highly unlikely. Such circumstances occur when working with high-frequency light. In the case of high frequency and off-resonant irradiation, we can obtain an effective static Floquet Hamiltonian as[87,88]

$$H_{\mathrm{eff}}=H_0+\frac{[H_1,H_{-1}]}{\omega l}+O(\omega^{-2}), \tag{5}$$

where the commutator $[H_1,\ H_{-1}]$ captures the leading order correction due to the periodic driving.

3. DSM under CPL propagating along the z-direction

In the presence of CPL propagating along the z direction, we derive an effective Floquet Hamiltonian by using Eq. (5), which reads

$$H_{\mathrm{eff}}^z=\sum_{i=1}^{5}H_i^z\Gamma_i+\sum_{i,j=1}^{5}H_{ij}^z\Gamma_{ij}, \tag{6}$$

where $\Gamma_{ij}=[\Gamma_i,\Gamma_j]/(2\mathrm{i})$, and the precise expressions of H_i^z and H_{ij}^z are given in Appendix A. The CPL breaks TRS while preserving inversion symmetry and the two-fold rotational symmetry C_{2z}. Each Dirac point splits into a pair of Weyl points [see Fig 2(a)] due to the breaking of TRS, resulting in a Floquet WSM with two pairs of Weyl nodes. To unveil the topological surface states, we plot the spectral function in the surface Brillouin zone on the k_2–k_z plane with a semi-infinite boundary along the x direction in Fig. 2(b). We observe the emergence of surface Fermi arcs terminating at the projections of each pair of Weyl nodes. Concurrently, the closed Fermi ring of the DSM is inherited by the Floquet WSM, existing between the two pairs of Weyl nodes. Moreover, the Floquet WSM exhibits HOFA states, which connect the projections of two adjacent Weyl nodes from two different pairs. This is illustrated by the band structure drawing with OBC along both x and y directions, and a periodic condition along the z-direction, as shown in Fig. 2(c). Figure 2(d) shows the 2D spatial distribution of the hinge Fermi arc state at a specific k_z slice. Evidently, these hinge Fermi arcs are located on the six hinges of the hexagonal disk.

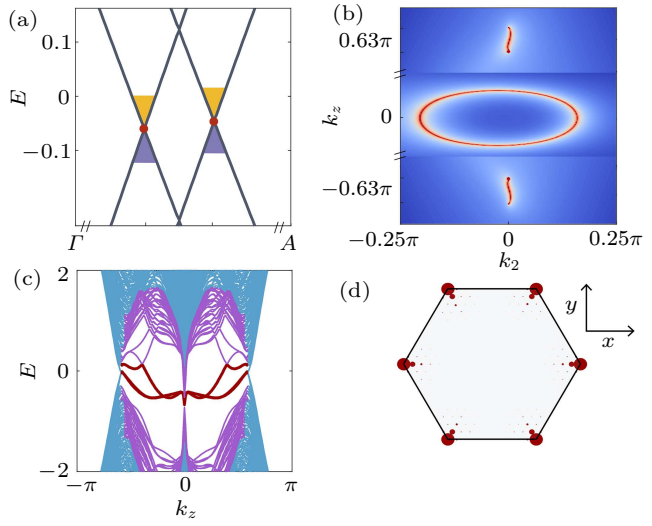


Fig. 2. The electronic structure of the Floquet WSM induced by the CPL propagating along the z-direction. (a) The bulk spectrum near the pair of Weyl points. The red dots denote the pair of Weyl points. (b) The spectral function of surface Fermi arcs and the surface Fermi ring states on the k_2–k_z plane when $E=-0.035$. The four red dots are the two pairs of Weyl points. (c) The energy spectrum as a function of k_z for the OBC along both the x and y directions. The red lines indicate hinge Fermi arc states between two adjacent Weyl nodes from different pairs. The purple lines are gapless surface states. (d) The LDOS of the hinge Fermi arc state of $k_z=0.02\pi$ on the x–y plane. The parameters are chosen as $M_0=4,M_1=-2.5,M_2=-1,\lambda=1,\gamma=5,m_0=-0.4,m_1=-0.1,m_2=0.05,A=0.5,\omega=8$.

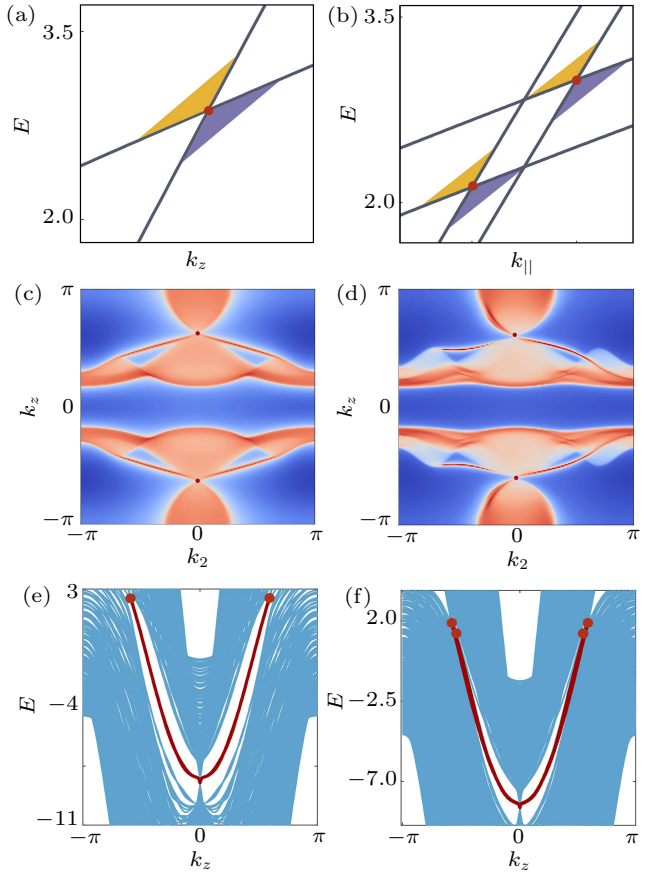


Fig. 3. Undriven type-II DSM and Floquet type-II WSM induced by CPL propagating along the z direction. (a) The bulk Dirac cone of the type-II DSM with $|m_1|/|M_1| = 1.6$. The red dot marks the Dirac point. The yellow and blue triangles represent the electron pocket and hole pocket, respectively. (b) The Dirac cone splits to a pair of Weyl cones of the type-II WSM for $A = 0.5$, and $\omega = 8$. (c) and (d) The spectral function on the k_2–k_z plane of type-II DSM and WSM with the OBC along the x axis when $E = 3.1$ and $E = 2.38$. The additional red curves near Weyl points are the surface Fermi arcs. (e) and (f) The energy spectrum versus k_z with the OBCs along the x and y directions. The solid red lines represent the hinge Fermi arc states. The parameters are chosen as $M_0 = 4$, $M_1 = -2.5$, $m_1 = -4$, $M_2 = -1$, $\lambda = 1$, $\gamma = 5$, $m_0 = -0.4$, $m_2 = 0.05$.

We now explore the tilting of Dirac cones in the influence of CPL, which is governed by the ratio of $|m_1|$ and $|M_1|$. The type-I DSM is characterized by $|m_1/M_1| < 1$, while the type-II DSM has $|m_1/M_1| > 1$ and exhibits over-tilted Dirac cones. Furthermore, a critical state exists between the type-I and type-II DSMs when $|m_1/M_1| = 1$. Figures 3(a) and 3(b) illustrate the over-tilted Dirac node transition to the Weyl nodes by CPL, respectively. We find that CPL along the z-direction does not alter the tilting degree of Dirac cone, resulting in Floquet WSMs retaining the same type as their parent DSMs. Additionally, we compare the surface states of the parent type-II DSM with those of the Floquet type-II WSM in Figs. 3(c) and 3(d). Unlike the Floquet type-I WSM, which has a point like Fermi surface, the tilting of Weyl cones in the type-II case leads to the coexistence of electron and hole pockets that meet at the Weyl nodes. The closed Fermi ring in the type-I case evolves into four segments of Fermi arcs. Meanwhile, the surface Fermi arcs emerge in between the Weyl nodes within the same pair in the Floquet WSM (see the dark red lines at the edges of the Fermi surfaces in Fig. 3(d)). Furthermore, the Floquet type-II WSM also hosts the hinge Fermi arc states as the type-II DSM, although they are deeply embedded within the bulk states, as shown in Figs. 3(e) and 3(f). Note that the hinge Fermi arcs in the Floquet WSM connect the two Weyl nodes, whereas in the DSM they connect the two Dirac cones.

To better understand the results derived from the discrete lattice model, we turn to the continuous low-energy model under periodic driving. The low-energy continuous DSM Hamiltonian in the vicinity of the Dirac point $\boldsymbol{K}_0 = (0,0,k^0_{z\pm})$ can be expressed as

$$\begin{aligned} H(\boldsymbol{q}) \;=\; & [(m_0+6m_2)-\frac{3}{2}m_2(q_x^2+q_y^2)-2m_1q_zK_1 \\ & -m_1(-2+q_z^2)K_2]+3\lambda(-q_x\Gamma_1+q_y\Gamma_2) \\ & +[(M_0+6M_2)-\frac{3}{2}M_2(+q_x^2+q_y^2)-2M_1q_zK_1 \\ & -M_1(-2+q_z^2)K_2]\Gamma_3+\frac{3}{4}\gamma(-q_x^2+q_y^2)K_1\Gamma_4 \\ & +\frac{3}{2}\gamma q_xq_yK_1\Gamma_5, \end{aligned} \tag{7}$$

where $\boldsymbol{q} = \boldsymbol{k} - \boldsymbol{K}_0$ is the wave vector measured from the Dirac nodes, $K_1 = \sin k_z^0$ and $K_2 = \cos k_z^0$. In the following results, we set $k_z^0 = \pi/2$ for simplicity. The energy dispersion to the leading order is

$$\begin{aligned} T(\boldsymbol{q}) \;&=\; -2m_1q_z, \\ U(\boldsymbol{q}) \;&=\; -\sqrt{3[3\lambda^2-M_2(m_0+6M_2)](q_x^2+q_y^2)+4M_1^2q_z^2}, \end{aligned} \tag{8}$$

where $T(\boldsymbol{q})$ represents the tilting energy, while $U(\boldsymbol{q})$ describes the splitting of the Dirac cone. When the energy U is predominant, the node is classified as type I. Conversely, when the energy T surpasses U, the node becomes type II. In the present case, the Dirac cone is tilted along the z direction. Therefore, the type of Dirac point can be determined by the ratio $|T(\boldsymbol{q})/U(\boldsymbol{q})|$, $|T(\boldsymbol{q})/U(\boldsymbol{q})| = |T(q_z)/U(q_z)| = |m_1/M_1|$. When the ratio is less than 1, it corresponds to a type I Dirac cone, reaching a critical state when it equals 1. Once the ratio exceeds 1, it manifests a type II Dirac cone. The introduction of a periodic driving field in the continuous Hamiltonian is achieved through the minimal coupling $\boldsymbol{q} \to \boldsymbol{q} - \boldsymbol{A}$. In the high-frequency regime,[87] the undriven Hamiltonian experiences a correction

$$\begin{aligned} \Delta H^z(\boldsymbol{q}) \;=\; & \frac{A^2e^2\eta}{\hbar\omega}\{9\lambda M_2(q_x\Gamma_{23}+q_y\Gamma_{13})-\frac{9\gamma M_2}{2}K_1 \\ & \times[(q_x^2-q_y^2)\Gamma_{35}+2q_xq_y\Gamma_{34}]+\frac{9}{2}\lambda\gamma K_1 \\ & \times[q_x(-\Gamma_{15}+\Gamma_{24})-q_y(\Gamma_{25}+\Gamma_{14})] \\ & -\frac{3}{4\eta}[2\hbar\omega M_2\Gamma_3+12\lambda^2\Gamma_{12}\eta \\ & +3\gamma^2\eta{K_1}^2(q_x^2+q_y^2)\Gamma_{45}]\}. \end{aligned} \tag{9}$$

The correction split each Dirac cone into two Weyl nodes along the q_z direction at $\boldsymbol{q}_z^0 = (0, 0, Q_z^{1,2})$

$$Q_z^{1,2} = \frac{3e^2A^2(\pm 6\lambda^2 - M_2\hbar\omega)}{4M_1\hbar\omega} + \frac{m_0 + 6M_2}{2M_1}. \tag{10}$$

Note that the correction has no effect on the tilting of Weyl cone.

4. DSM under CPL propagating in the *x*-direction

In the presence of CPL propagating along the x direction, we can also obtain an effective Hamiltonian

$$H_{\text{eff}}^x = \sum_{i=1}^{5} H_i^x \Gamma_i + \sum_{i,j=1}^{5} H_{ij}^x \Gamma_{ij}. \tag{11}$$

The precise expressions of H_i^x and H_{ij}^x are provided in the Appendix B. The situation when CPL propagates along the x direction is analogous to the case of CPL propagating along the z direction, where the original hopping terms are renormalized, and next-nearest-neighbor hopping terms are induced. Additionally, it also gives rise to more distant hopping terms on the y–z plane. The photoinduced Weyl nodes emerge on the k_1–k_z plane in the reciprocal space, with one of the Weyl nodes depicted in Fig. 4(a). In this scenario, the Floquet WSM also exhibits a surface Fermi ring surrounding an electron Fermi pocket, around the Γ point, as illustrated in Figs. 4(b) and 4(c),

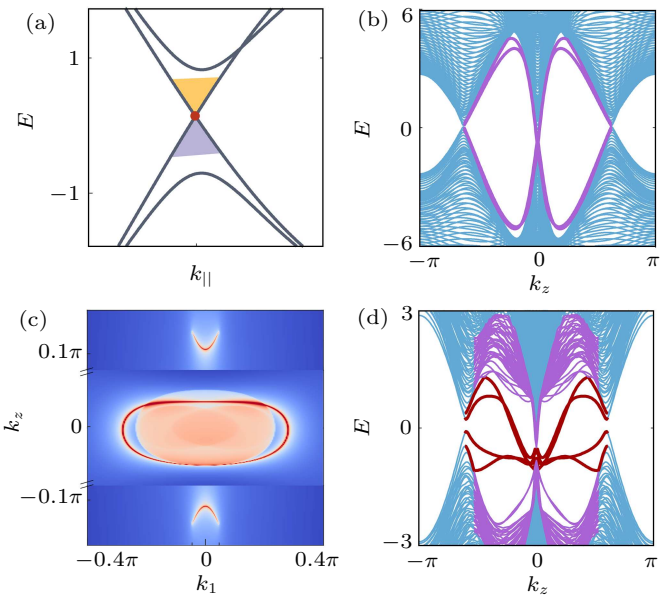


Fig. 4. The electronic structure of the Floquet WSM induced by the CPL propagating along the x-direction. (a) The bulk spectrum around one of the Weyl cones of the Floquet WSM. The red dot denotes the Weyl point. The yellow and blue triangles represent the conduction band and valence band. (b) The surface band structure versus k_z at $k_y = 0$. The purple solid lines show the gapless surface state between the two adjacent Weyl points. (c) The spectral function on the k_1–k_z plane with the semi-infinite boundary along the y direction when $E = 0.1$. (d) The band spectrum for the hinge states with OBC along both the x and y directions. The red lines indicate hinge Fermi arc states between two adjacent Weyl nodes from different pairs. The purple lines are gapless surface states. The parameters are chosen as $M_0 = 4$, $M_1 = -2.5$, $M_2 = -1$, $\lambda = 1$, $\gamma = 5$, $m_0 = -0.4$, $m_1 = -0.1$, $m_2 = 0.05$, $A = 0.5$, $\omega = 6$.

as well as surface Fermi arc states terminating at the projections of the Weyl nodes in the surface Brillouin zone, as shown in Fig. 4(c). Furthermore, the Floquet WSM also manifests hinge Fermi arc states, which can be observed in the band structure calculated with OBC along both x and y directions and periodic boundary condition along z-direction [Fig. 4(d)].

Of particular significance, the CPL propagating along the x-direction profoundly impacts the tilting of the Dirac cone, enabling the transformation of a parent type-I DSM into a Floquet type-II WSM by modulating the amplitude of CPL. To elucidate this phenomenon, we start with a type-I DSM in which the ratio $|m_1/M_1|$ governing the tilt of Dirac cone is close to unity. Figure 5(a) represents the tilted Dirac cone in a type-I DSM, whereas Fig. 5(b) depicts one of the over-tilted Weyl cones induced by the CPL. The surface states of the photoinduced type-II WSM are shown in Fig. 5(c). Figure 5(d) plots the hinge Fermi arc states deeply embedded in the bulk states. To comprehend the underlying mechanism by which the CPL propagating along the x-direction, rather than the z-direction, induces a type-II WSM from a type-I DSM, we examine the low-energy continuous DSM Hamiltonian under periodic driving. The CPL propagating along the x-direction introduces a correction to the undriven DSM Hamiltonian, which is given by

$$\begin{aligned}\Delta H^x(\boldsymbol{q}) = {} & \frac{3e^2A^2M_1}{\hbar\omega}[-2\lambda\eta(q_z g_2 + g_1)\Gamma_{23} \\ & + \gamma\eta(q_x g_1(q_z g_2 + g_1)\Gamma_{35} + q_y g_1(q_z g_2 + g_1)\Gamma_{34})] \\ & - \left(\frac{e^2A^2M_1}{2} g_2 + \frac{3M_2e^2A^2}{4}\right)\Gamma_3 + \frac{3\gamma e^2A^2}{8} g_1\Gamma_4,\end{aligned} \tag{12}$$

where $\boldsymbol{q} = \boldsymbol{k} - \boldsymbol{K}_0$ is the wave vector measured from the Dirac nodes, and $g_1 = \sin k_z^0$ and $g_2 = \cos k_z^0$. In our calculations, k_z^0 is fixed at $\pi/2$. This correction leads to each Dirac point being separated into a pair of Weyl nodes located at $\boldsymbol{q}^0 = (\pm\xi Q_z, 0, \pm Q_z)$, where ξ and Q_z depend on the amplitude and frequency of CPL. The tilting energy in this case is given by $T(q) = 2m_1 q_z + 3\xi Q_z m_2 q_x$. To characterize the tilting degree of the Weyl cones, We perform a rotation to the tilting direction $\boldsymbol{q}' = R[\theta_q = \tan^{-1}(-2M_1/(3\xi Q_z M_2))]\boldsymbol{q}$, resulting in $T(q)$ being proportional to q_z'. Now the tilting ratio reads

$$\left|\frac{T(q_z')}{U(q_z')}\right| = \left|\frac{m_1}{M_1}\right| \frac{1 + (\xi Q_z \Delta m)^2}{\sqrt{(1 + \xi^2 Q_z^2 \Delta m \Delta M)^2 + {g_A}^2}}, \tag{13}$$

where $\Delta m = m_2/m_1$, $\Delta M = M_2/M_1$, and g_A is determined by the amplitude of CPL A and the model parameters λ, γ, m_0. Evidently, the CPL propagating along the x-direction not only splits the Dirac nodes into pairs of Weyl nodes, but also renormalizes the tilting ratio. For an initial tilting ratio $|m_1/M_1| < 1$, a Floquet type-II WSM can be realized by adjusting the amplitude of CPL propagating along the x-direction. We also study

the DSM under the CPL propagating along the y-direction, the results are quite similar to the case of CPL propagating along the x-direction.

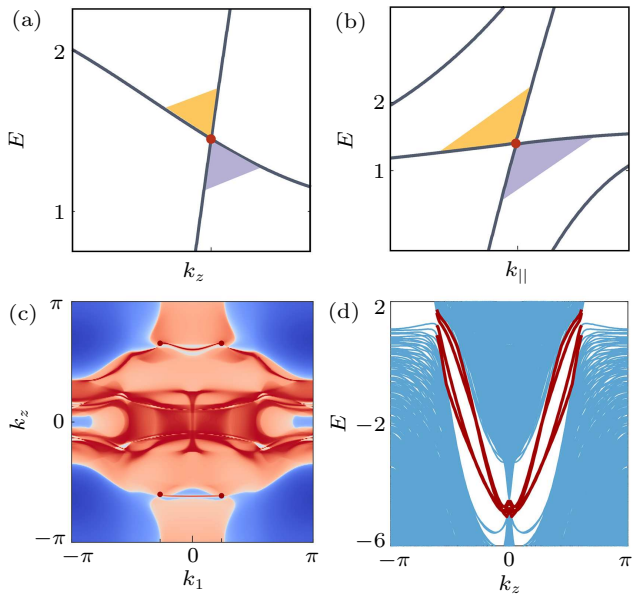


Fig. 5. Tilting effect in the presence of CPL propagating along x direction. (a) The bulk band structure near one of the Dirac nodes in a type-I DSM. The red point marks the Dirac point. The yellow and purple triangles represent the conduction band and valence band, respectively. (b) The bulk band structure near one of the photoinduced Weyl nodes in the type-II WSM. The red point is one of the Weyl points. The amplitude of the applied light is $A = 0.9$. (c) The spectral function on the k_1–k_z plane of the type-II WSM with the OBC along the x axis when $E = 1.68$. The red dots are projections of four Weyl points. (d) The hinge spectrum of the type-II WSM with the OBC along the x and y axis. The solid red lines represent the hinge Fermi arc state. The parameters are chosen as $M_0 = 4$, $M_1 = -2.5$, $M_2 = -1$, $\lambda = 1$, $\gamma = 5$, $m_0 = -0.4$, $m_1 = -2.1$, $m_2 = 0.05$, $A = 0.9$, $\omega = 6$.

5. Discussion and conclusion

In this work, we have investigated the C_6 symmetric DSM under off-resonant CPL with distinct propagation directions. In the framework of Floquet theory, we unveiled the emergence of Floquet WSMs boasting diverse boundary states, including surface Fermi arcs and hinge Fermi arc states. It is important to note that the γ terms in the original Dirac semimetal Hamiltonian play a crucial role in determining the higher-order topology, and consequently, the emergence of HOFA states. In the absence of these terms, the Dirac semimetal exhibits only helical surface Fermi arc states. Under CPL, a Floquet Weyl semimetal also emerges; however, chiral hinge Fermi arc states are absent. Notably, we demonstrated the controllable modulation of photoinduced Weyl cones by adjusting both the incident direction and amplitude of CPL. These findings not only shed light on the intricate interplay between light-induced effects and material symmetry but also pave the way for engineering Floquet WSMs endowed with higher-order topological characteristics. Thus, our work presents a promising avenue towards harnessing tailored topological states in condensed matter systems through Floquet engineering techniques.

Appendix A: The effective Floquet Hamiltonian for CPL propagating along the z-direction

Within the context of circularly polarized light propagating along the z-axis, we can derive an effective static Floquet Hamiltonian in the high-frequency regime

$$H^z_{\rm eff} = \sum_{i=1}^{5} H^z_i \Gamma_i + \sum_{i,j=1}^{5} H^z_{ij} \Gamma_{ij}, \tag{A1}$$

with the components of H^z_i and H^z_{ij} being given by

$$\begin{aligned}
H^z_0 &= m_0 + 2m_1 \cos k_z + 2m_2 J_0(A)[\cos k_3 + \cos k_2 + \cos k_1],\\
H^z_1 &= \lambda J_0(A)[\sin k_2 + \sin k_3 - 2\sin k_1],\\
H^z_2 &= \sqrt{3}\lambda J_0(A)[-\sin k_3 + \sin k_2],\\
H^z_3 &= M_0 + 2M_1 \cos k_z + 2M_2 J_0(A)[\cos k_3 \cos k_2 + \cos k_1],\\
H^z_4 &= 2\gamma \sin k_z J_0(L)\Big\{\cos k_1 - \frac{1}{2}[\cos k_3 + \cos k_2]\Big\},\\
H^z_5 &= \sqrt{3}\gamma \sin k_z J_0(A)[\cos k_2 - \cos k_3],\\
H^z_{12} &= \frac{2J_1(A)^2}{\omega} 3\lambda^2 [\cos k_1 + \cos k_{n1} - \cos k_2\\
&\quad - \cos k_{n3} - \cos k_3 - \cos k_{n2}],\\
H^z_{13} &= -\frac{2J_1(A)^2}{\omega} \sqrt{3} M_2 \lambda [3\sin k_3 + 2\sin k_{n1}\\
&\quad - 3\sin k_2 - 3\sin k_{n3} - \sin k_{n2}],\\
H^z_{14} &= \frac{2J_1(A)^2}{\omega} \sqrt{3}\lambda\gamma \sin k_z [-2\sin k_{n3}\\
&\quad - 2\sin k_{n2} + \sin k_{n1}],\\
H^z_{15} &= -\frac{2J_1(A)^2}{\omega} 3\lambda\gamma \sin k_z [-\sin k_{n3} + \sin k_3\\
&\quad + \sin k_{n2} + \sin k_2 - \sin k_1],\\
H^z_{23} &= \frac{2J_1(A)^2}{\omega} 6M_2\lambda \Big\{-\sin k_1 + \frac{1}{2}[-\sin k_{n3}\\
&\quad - \sin k_3 + \sin k_{n2} - \sin k_2]\Big\},\\
H^z_{24} &= -\frac{2J_1(A)^2}{\omega} 3\lambda\gamma \sin k_z [-\sin k_1 + \sin k_{n3}\\
&\quad + \sin k_3 - \sin k_{n2} + \sin k_2],\\
H^z_{25} &= \frac{2J_1(A)^2}{\omega} 3\sqrt{3}\lambda\gamma \sin k_z \sin k_{n1},\\
H^z_{34} &= -\frac{2J_1(A)^2}{\omega} 3\sqrt{3} M_2 \gamma \sin k_z\\
&\quad \times [\cos k_{n3} - \cos k_3 - \cos k_{n2} + \cos k_2],\\
H^z_{35} &= \frac{2J_1(A)^2}{\omega} 3M_2\gamma \sin k_z [\cos k_{n3} - \cos k_3 + \cos k_{n2}\\
&\quad + 2\cos k_{n1} - \cos k_2 - 2\cos k_1],\\
H^z_{45} &= \frac{2J_1(A)^2}{\omega} 3\gamma^2 \sin^2 k_z [\cos k_{n3} - \cos k_3 + \cos k_{n2}\\
&\quad - \cos k_{n1} - \cos k_2 + \cos k_1],
\end{aligned} \tag{A2}$$

where $J_l(A)$ is the Bessel function of the l-th order, $l = 0, 1$, $\Gamma_{ij} = [\Gamma_i, \Gamma_j]/(2\mathrm{i})$. For simplicity, we introduce the notations $k_{n1} = k_2 - k_3$, $k_{n2} = k_1 - k_3$, $k_{n3} = k_2 - k_1$, and $k_3 = -k_1 - k_2$.

Appendix B: Light-driven DSM in the *x*-direction

In the presence of CPL propagating along the x direction, we also obtain an effective Floquet Hamiltonian according to Floquet's theorem, which reads

$$H^x_{\rm eff} = \sum_{i=1}^{5} H^x_i \Gamma_i + \sum_{i,j=1}^{5} H^x_{ij}\Gamma_{ij}, \tag{B1}$$

with the components of H^x_i and H^x_{ij} being expressed as

$$H^x_0 = m_0 + 2m_1 J_0(A)\cos k_z + 2m_2\left[J_0\left(\frac{A}{2}\right)\cos k_3 + J_0\left(\frac{A}{2}\right)\cos k_2 + J_0(A)\cos k_1\right],$$

$$H^x_1 = \lambda J_0\left(\frac{A}{2}\right)[\sin k_2 + \sin k_3] - 2\lambda J_0(A)\sin k_1,$$

$$H^x_2 = \lambda\sqrt{3}J_0\left(\frac{A}{2}\right)[-\sin k_3 + \sin k_2],$$

$$H^x_3 = M_0 + 2M_1 J_0(A)\cos k_z + 2M_2\left[J_0\left(\frac{A}{2}\right)\cos k_3 + J_0\left(\frac{A}{2}\right)\cos k_2 + J_0(A)\cos k_1\right];$$

$$H^x_4 = 2\gamma J_0(\sqrt{2}A)\sin k_z\cos k_1 - \gamma J_0\left(\frac{\sqrt{5}A}{2}\right)\sin k_z\cos k_3 - \gamma J_0\left(\frac{\sqrt{5}A}{2}\right)\sin k_z\cos k_2,$$

$$H^x_5 = \sqrt{3}\gamma J_0\left(\frac{\sqrt{5}A}{2}\right)\sin k_z[-\cos k_3 + \cos k_2],$$

$$\begin{aligned}H^x_{13} = {}& -8\lambda M_1 J_1(A)^2[\sin(k_1-k_z) - \sin(k_1+k_z)] - 4\lambda M_1 J_1\left(\frac{A}{2}\right)J_1(A)\,[\sin(k_2-k_z) + \sin(k_3-k_z) - \sin(k_2+k_z)\\ & - \sin(k_3+k_z)],\end{aligned}$$

$$\begin{aligned}H^x_{14} = {}& 2\lambda\gamma J_1(A)J_1\left(\frac{\sqrt{5}A}{2}\right)\sin\varphi\,[\cos(-k_{n3}-k_z) + \cos(-k_3-k_z) + \cos(k_{n2}-k_z) + \cos(-k_2-k_z) + \cos(-k_{n3}+k_z)\\ & + \cos(-k_3+k_z) + \cos(k_{n2}+k_z) + \cos(-k_2+k_z)] + 2\lambda\gamma J_1\left(\frac{A}{2}\right)J_1\left(\frac{\sqrt{5}A}{2}\right)\sin\varphi\left[\cos(k_{n1}-k_z) + \frac{1}{2}\cos(2k_2-k_z)\right.\\ & + \cos(-k_1-k_z) + \frac{1}{2}\cos(2k_3-k_z) + 2\cos(k_z) + \frac{1}{2}\cos(2k_2+k_z) + \cos(k_{n1}+k_z) + \cos(-k_1+k_z)\\ & \left.+\frac{1}{2}\cos(2k_3+k_z)\right] + 2\sqrt{2}\lambda\gamma J_1(A)J_1(\sqrt{2}A)[-\cos(2k_1-k_z) - 2\cos k_z - \cos(2k_1+k_z)] + \sqrt{2}\lambda\gamma J_1\left(\frac{A}{2}\right)J_1(\sqrt{2}A)\\ & \times[-\cos(-k_{n3}-k_z) - \cos(-k_3-k_z) - \cos(k_{n2}-k_z) - \cos(-k_2-k_z) - \cos(-k_{n3}+k_z) - \cos(-k_3+k_z)\\ & - \cos(k_{n2}+k_z) - \cos(-k_2+k_z)],\end{aligned}$$

$$\begin{aligned}H^x_{15} = {}& 2\sqrt{3}\lambda\gamma J_1(A)J_1\left(\frac{\sqrt{5}A}{2}\right)\sin\varphi\,[-\cos(-k_{n3}-k_z) - \cos(-k_3-k_z) + \cos(k_{n2}-k_z) + \cos(-k_2-k_z)\\ & - \cos(k_1-k_2+k_z) - \cos(-k_3+k_z) + \cos(k_{n2}+k_z) + \cos(-k_2+k_z)] - \sqrt{3}\lambda\gamma J_1\left(\frac{A}{2}\right)J_1\left(\frac{\sqrt{5}A}{2}\right)\sin\varphi\\ & \times[\cos(2k_2-k_z) + \cos(2k_3-k_z) - \cos(2k_2+k_z) + \cos(2k_3+k_z)],\end{aligned}$$

$$H^x_{23} = -4\sqrt{3}\lambda M_1 J_1\left(\frac{A}{2}\right)J_1(A)[\sin(k_2-k_z) - \sin(k_3-k_z) - \sin(k_2+k_z) + \sin(k_3+k_z)],$$

$$\begin{aligned}H^x_{24} = {}& -\sqrt{6}\lambda\gamma J_1\left(\frac{A}{2}\right)J_1(\sqrt{2}A)\,[\cos(-k_{n3}-k_z) + \cos(-k_3-k_z) - \cos(k_{n2}-k_z) - \cos(-k_2-k_z) + \cos(-k_{n3}+k_z)\\ & + \cos(-k_3+k_z) - \cos(k_{n2}+k_z) - \cos(-k_2+k_z)] + \lambda\gamma\sin\varphi J_1\left(\frac{A}{2}\right)J_1\left(\frac{\sqrt{5}A}{2}\right)\sqrt{3}\,[\cos(2k_2-k_z) - \cos(2k_3-k_z)\\ & + \cos(2k_2+k_z) - \cos(2k_3+k_z)],\end{aligned}$$

$$\begin{aligned}H^x_{25} = {}& 6\lambda\gamma J_1\left(\frac{A}{2}\right)J_1\left(\frac{\sqrt{5}A}{2}\right)\sin\varphi\left[-\frac{1}{2}\cos(2k_2-k_z) + \cos(k_{n1}-k_z) + \cos(-k_1-k_z) - \frac{1}{2}\cos(2k_3-k_z) - 2\cos kz\right.\\ & \left.-\frac{1}{2}\cos(2k_2+k_z) + \cos(k_{n1}+k_z) + \cos(-k_1+k_z) - \frac{1}{2}\cos(2k_3+k_z)\right],\end{aligned}$$

$$H^x_{34} = -2\sqrt{2}\gamma M_1 J_1(A)J_1(\sqrt{2}A)[2\sin k_1 - \sin(k_1-2k_z) + \sin(2k_1-k_z) + \sin(2k_1+k_z) - \sin(k_1+2k_z)]$$

$$
\begin{aligned}
&-2\gamma M_1 J_1(A) J_1\left(\frac{\sqrt{5}A}{2}\right)\cos\varphi[2\sin k_2+2\sin k_3-\sin(k_2-2k_z)-\sin(k_3-2k_z)-\sin(k_2+2k_z)-\sin(k_3+2k_z)]\\
&+2\gamma M_2 J_1(A) J_1\left(\frac{\sqrt{5}A}{2}\right)[\sin(-k_{n3}-k_z)+\sin(-k_3-k_z)+\sin(-k_{n3}+k_z)+\sin(-k_3+k_z)]\sin\varphi\\
&+2\gamma M_2 J_1(A) J_1\left(\frac{\sqrt{5}A}{2}\right)[\sin(k_{n2}-k_z)+\sin(-k_2-k_z)+\sin(k_{n2}+k_z)+\sin(-k_2+k_z)]\sin\varphi\\
&-2(\sqrt{2}\gamma M_2 J_1\left(\frac{A}{2}\right)J_1(\sqrt{2}A)\ [\sin(-k_{n3}-k_z)-\sin(-k_3-k_z)+\sin(k_{n2}-k_z)-\sin(-k_2-k_z)+\sin(-k_{n3}+k_z)\\
&-\sin(-k_3+k_z)+\sin(k_{n2}+k_z)-\sin(-k_2+k_z)]+2\gamma M_2 J_1\left(\frac{A}{2}\right)J_1\left(\frac{\sqrt{5}A}{2}\right)[\sin(2k_2-k_z)-2\sin(-k_1-k_z)\\
&-\sin(2k_3-k_z)+\sin(2k_2+k_z)-2\sin(-k_1+k_z)-\sin(2k_3+k_z))\sin\varphi],\\
H_{35}^{x}=&\,2\sqrt{3}\gamma M_2 J_1(A) J_1\left(\frac{\sqrt{5}A}{2}\right)\sin\varphi[-\sin(-k_{n3}-k_z)-\sin(-k_3-k_z)+\sin(k_{n2}-k_z)+\sin(-k_2-k_z)\\
&-\sin(-k_{n3}+k_z)-\sin(-k_3+k_z)+\sin(k_{n2}+k_z)+\sin(-k_2+k_z)]+2\sqrt{3}\gamma M_2 J_1\left(\frac{A}{2}\right)J_1\left(\frac{\sqrt{5}A}{2}\right)\sin\varphi\\
&\times[\sin(2k_2-k_z)-2\sin(k_{n1}-k_z)-\sin(2k_3-k_z)+\sin(2k_2+k_z)-2\sin(k_{n1}+k_z)-\sin(2k_3+k_z)]\\
&+2\sqrt{3}\cos\varphi M_1\gamma J_1(A) J_1\left(\frac{\sqrt{5}A}{2}\right)[2\sin k_2-2\sin k_3-\sin(k_2-2k_z)+\sin(k_3-2k_z)-\sin(k_2+2k_z)\\
&+\sin(k_3+2k_z)],\\
H_{45}^{x}=&\,\gamma^2 J_1\left(\frac{\sqrt{5}A}{2}\right)^2\sqrt{3}\sin 2\varphi[\cos(k_{n1}-2k_z)-\cos(k_{n1}+2k_z)]+\sqrt{6}\gamma^2 J_1(\sqrt{2}A)J_1\left(\frac{\sqrt{5}A}{2}\right)[-\cos(-k_{n3}-2k_z)\\
&-\cos(-k_3-2k_z)+\cos(k_{n2}-2k_z)+\cos(-k_2-2k_z)+\cos(-k_{n3}+2k_z)+\cos(-k_3+2k_z)-\cos(k_{n2}+2k_z)\\
&-\cos(-k_2+2k_z)]\sin\varphi+\sqrt{6}\gamma^2 J_1(\sqrt{2}A)J_1\left(\frac{\sqrt{5}A}{2}\right)\cos\varphi[\cos(-k_{n3}-2k_z)-\cos(-k_3-2k_z)-\cos(k_{n2}-2k_z)\\
&+\cos(-k_2-2k_z)-\cos(-k_{n3}+2k_z)+\cos(-k_3+2k_z)+\cos(k_{n2}+2k_z)-\cos(-k_2+2k_z)].
\end{aligned}
\tag{B2}
$$

Acknowledgements

Project supported by the National Key R&D Program of China (Grant No. 2022YFA1403700), the National Natural Science Foundation of China (Grant Nos. 12074108 and 12347101), the Chongqing Natural Science Foundation (Grant No. CSTB2022NSCQ-MSX0568), the Fundamental Research Funds for the Central Universities (Grant No. 2023CDJXY048), the Natural Science Foundation of Jiangsu Province (Grant No. BK20230066), and the Jiangsu Shuang Chuang Project (Grant No. JSSCTD202209).

References

[1] Burkov A 2016 *Nat. Mater.* **15** 1145
[2] Burkov A A, Hook M D and Balents L 2011 *Phys. Rev. B* **84** 235126
[3] Yang B J and Nagaosa N 2014 *Nat. Commun.* **5** 4898
[4] Armitage N P, Mele E J and Vishwanath A 2018 *Rev. Mod. Phys.* **90** 015001
[5] Wang Z, Sun Y, Chen X Q, Franchini C, Xu G, Weng H, Dai X and Fang Z 2012 *Phys. Rev. B* **85** 195320
[6] Wang Z, Weng H, Wu Q, Dai X and Fang Z 2013 *Phys. Rev. B* **88** 12542
[7] Kargarian M, Randeria M and Lu Y M 2016 *Proc. Natl. Acad. Sci. USA* **113** 8648
[8] Wieder B J, Bradlyn B, Cano J, Wang Z, Vergniory M G, Elcoro L, Soluyanov A A, Felser C, Neupert T and Regnault N 2022 *Nat. Rev. Mater.* **7** 196
[9] Le C, Wu X, Qin S, Li Y, Thomale R, Zhang F C and Hu J 2018 *Proc. Natl. Acad. Sci. USA* **115** 8311
[10] Lin M and Hughes T L 2018 *Phys. Rev. B* **98** 241103(R)
[11] Wieder B J, Wang Z, Cano J, Dai X, Schoop L M, Bradlyn B and Bernevig B A 2020 *Nat. Commun.* **11** 1
[12] Fang Y and Cano J 2021 *Phys. Rev. B* **104** 245101
[13] Tyner A C, Sur S, Zhou Q, Puggioni D, Darancet P, Rondinelli J M and Goswami P 2021 arXiv:2102.06207v2
[14] Nie S, Chen J, Yue C, Le C, Yuan D, Wang Z, Zhang W and Weng H 2022 *Science Bulletin* **67** 1958
[15] Zeng X T, Chen Z, Chen C, Liu B B, Sheng X L and Yang S A 2023 *Front. Phys* **18** 13308
[16] Eckardt A 2017 *Rev. Mod. Phys.* **89** 011004
[17] de la Torre A, Kennes D M, Claassen M, Gerber S, McIver J W and Sentef M A 2021 *Rev. Mod. Phys.* **93** 041002
[18] Weitenberg C and Simonet J 2021 *Nat. Phys.* **17** 1342
[19] Cayssol J, Dóra B, Simon F and Moessner R 2013 *Phys. Status Solidi RRL* **7** 101
[20] Oka T and Kitamura S 2019 *Annu. Rev. Condens. Matter Phys.* **10** 387
[21] Harper F, Roy R, Rudner M S and Sondhi S 2020 *Annu. Rev. Condens. Matter Phys.* **11** 345
[22] Rudner M S and Lindner N H 2020 *Nat. Rev. Phys.* **2** 229
[23] Bao C, Tang P, Sun D and Zhou S 2022 *Nat. Rev. Phys.* **4** 33
[24] Oka T and Aoki H 2009 *Phys. Rev. B* **79** 081406
[25] Inoue J i and Tanaka A 2010 *Phys. Rev. Lett.* **105** 017401
[26] Kitagawa T, Berg E, Rudner M and Demler E 2010 *Phys. Rev. B* **82** 235114
[27] Gu Z, Fertig H A, Arovas D P and Auerbach A 2011 *Phys. Rev. Lett.* **107** 216601
[28] Kitagawa T, Oka T, Brataas A, Fu L and Demler E 2011 *Phys. Rev. B* **84** 235108

[29] Delplace P, Gómez-León A and Platero G 2013 *Phys. Rev. B* **88** 245422
[30] Foa Torres L E F, Perez-Piskunow P M, Balseiro C A and Usaj G 2014 *Phys. Rev. Lett.* **113** 266801
[31] Usaj G, Perez-Piskunow P M, Foa Torres L E F and Balseiro C A 2014 *Phys. Rev. B* **90** 115423
[32] Lindner N H, Refael G and Galitski V 2011 *Nat. Phys.* **7** 490
[33] Kitagawa T, Rudner M S, Berg E and Demler E 2010 *Phys. Rev. A* **82** 033429
[34] Lindner N H, Bergman D L, Refael G and Galitski V 2013 *Phys. Rev. B* **87** 235131
[35] Jiang L, Kitagawa T, Alicea J, Akhmerov A R, Pekker D, Refael G, Cirac J I, Demler E, Lukin M D and Zoller P 2011 *Phys. Rev. Lett.* **106** 220402
[36] Rudner M S, Lindner N H, Berg E and Levin M 2013 *Phys. Rev. X* **3** 031005
[37] Ezawa M 2013 *Phys. Rev. Lett.* **110** 026603
[38] Gómez-León A and Platero G 2013 *Phys. Rev. Lett.* **110** 200403
[39] Grushin A G, Gómez-León A and Neupert T 2014 *Phys. Rev. Lett.* **112** 156801
[40] Wang R, Wang B, Shen R, Sheng L and Xing D Y 2014 *Europhys. Lett.* **105** 17004
[41] Narayan A 2016 *Phys. Rev. B* **94** 041409
[42] Yan Z and Wang Z 2016 *Phys. Rev. Lett.* **117** 087402
[43] Taguchi K, Xu D H, Yamakage A and Law K T 2016 *Phys. Rev. B* **94** 155206
[44] González J and Molina R A 2016 *Phys. Rev. Lett.* **116** 156803
[45] Narayan A 2015 *Phys. Rev. B* **91** 205445
[46] Saha K 2016 *Phys. Rev. B* **94** 081103
[47] Chan C K, Oh Y T, Han J H and Lee P A 2016 *Phys. Rev. B* **94** 121106
[48] Yan Z and Wang Z 2017 *Phys. Rev. B* **96** 041206
[49] Zou J Y and Liu B G 2016 *Phys. Rev. B* **93** 205435
[50] Hübener H, Sentef M A, De Giovannini U, Kemper A F and Rubio A 2017 *Nat. Commun.* **8** 1
[51] Chen R, Zhou B and Xu D H 2018 *Phys. Rev. B* **97** 155152
[52] Zhang D, Wang H, Ruan J, Yao G and Zhang H 2018 *Phys. Rev. B* **97** 195139
[53] Firoz Islam S and Zyuzin A A 2019 *Phys. Rev. B* **100** 165302
[54] Deng T, Zheng B, Zhan F, Fan J, Wu X and Wang R 2020 *Phys. Rev. B* **102** 201105
[55] Ghosh A K, Nag T and Saha A 2022 *Phys. Rev. B* **105** 115418
[56] Nag T and Roy B 2021 *Commun. Phys.* **4** 1
[57] Nag T, Slager R J, Higuchi T and Oka T 2019 *Phys. Rev. B* **100** 134301
[58] Du X L, Chen R, Wang R and Xu D H 2022 *Phys. Rev. B* **105** L081102
[59] Trevisan T V, Arribi P V, Heinonen O, Slager R J and Orth P P 2022 *Phys. Rev. Lett.* **128** 066602
[60] Bomantara R W, Zhou L, Pan J and Gong J 2019 *Phys. Rev. B* **99** 045441
[61] Rodriguez-Vega M, Kumar A and Seradjeh B 2019 *Phys. Rev. B* **100** 085138
[62] Nag T, Juričić V and Roy B 2019 *Phys. Rev. Research* **1** 032045
[63] Seshadri R, Dutta A and Sen D 2019 *Phys. Rev. B* **100** 115403
[64] Peng Y and Refael G 2019 *Phys. Rev. Lett.* **123** 016806
[65] Hu H, Huang B, Zhao E and Liu W V 2020 *Phys. Rev. Lett.* **124** 057001
[66] Ghosh A K, Paul G C and Saha A 2020 *Phys. Rev. B* **101** 235403
[67] Peng Y 2020 *Phys. Rev. Research* **2** 013124
[68] Bomantara R W 2020 *Phys. Rev. Research* **2** 033495
[69] Huang B and Liu W V 2020 *Phys. Rev. Lett.* **124** 216601
[70] Zhu W, Chong Y D and Gong J 2021 *Phys. Rev. B* **103** L041402
[71] Zhang R X and Yang Z C 2021 *Phys. Rev. B* **103** L121115
[72] Nag T, Juričić V and Roy B 2021 *Phys. Rev. B* **103** 115308
[73] Zhu W, Chong Y D and Gong J 2021 *Phys. Rev. B* **104** L020302
[74] Zhu W, Umer M and Gong J 2021 *Phys. Rev. Research* **3** L032026
[75] Rui W B, Zhang S B, Hirschmann M M, Zheng Z, Schnyder A P, Trauzettel B and Wang Z D 2021 *Phys. Rev. B* **103** 184510
[76] Wang B Q, Wu H and An J H 2021 *Phys. Rev. B* **104** 205117
[77] Ghosh S, Saha K and Sengupta K 2022 *Phys. Rev. B* **105** 224312
[78] Wang Z M, Wang R, Sun J H, Chen T Y and Xu D H 2023 *Phys. Rev. B* **107** L121407
[79] Hu K, Qin Y, Cheng L, Shi Y and Qi J 2023 *Chin. Phys. Lett.* **40** 114202
[80] Gao L L and Huang X G 2022 *Chin. Phys. Lett.* **39** 021101
[81] Zheng Y, Chen W, Wan X and Xing D 2023 *Chin. Phys. Lett.* **40** 097301
[82] McIver J W, Schulte B, Stein F U, Matsuyama T, Jotzu G, Meier G and Cavalleri A 2020 *Nat. Phys.* **16** 38
[83] Liu Z, Zhou B, Zhang Y, Wang Z, Weng H, Prabhakaran D, Mo S K, Shen Z, Fang Z, Dai X, *et al.* 2014 *Science* **343** 864
[84] Roy B 2019 *Phys. Rev. Res.* **1** 032048
[85] Wang H X, Lin Z K, Jiang B, Guo G Y and Jiang J H 2020 *Phys. Rev. Lett.* **125** 146401
[86] Ghorashi S A A, Li T and Hughes T L 2020 *Phys. Rev. Lett.* **125** 266804
[87] Bukov M, D'Alessio L and Polkovnikov A 2015 *Adv. Phys.* **64** 139
[88] Eckardt A and Anisimovas E 2015 *New J. Phys.* **17** 093039